Title

Light-Controlled Multiphase Structuring of Perovskite Crystal Enabled by Thermoplasmonic Metasurface

Journal

ACS Nano, 17(10)

ISSN

1936-0851

Authors

Kharintsev, Sergey S
Battalova, Elina I
Mukhametzyanov, Timur A
et al.

Publication Date

2023-05-23

DOI

10.1021/acsnano.3c00373

ACS NANO

www.acsnano.org

ARTICLE

Light-Controlled Multiphase Structuring of Perovskite Crystal Enabled by Thermoplasmonic Metasurface

Sergey S. Kharintsev,* Elina I. Battalova, Timur A. Mukhametzyanov, Anatoly P. Pushkarev, Ivan G. Scheblykin, Sergey V. Makarov, Eric O. Potma, and Dmitry A. Fishman*

Cite This: *ACS Nano* 2023, 17, 9235–9244

Read Online

ACCESS | Metrics & More | Article Recommendations | Supporting Information

ABSTRACT: **Halide perovskites belong to an important family of semiconducting materials with electronic properties that enable a myriad of applications, especially in photovoltaics and optoelectronics. Their optical properties, including photoluminescence quantum yield, are affected and notably enhanced at crystal imperfections where the symmetry is broken and the density of states increases. These lattice distortions can be introduced through structural phase transitions, allowing charge gradients to appear near the interfaces between phase structures. In this work, we demonstrate controlled multiphase structuring in a single perovskite crystal. The concept uses cesium lead bromine ($CsPbBr_3$) placed on a thermoplasmonic TiN/Si metasurface and enables single-, double-, and triple-phase structures to form on demand above room temperature. This approach promises application horizons of dynamically controlled heterostructures with distinctive electronic and enhanced optical properties.**

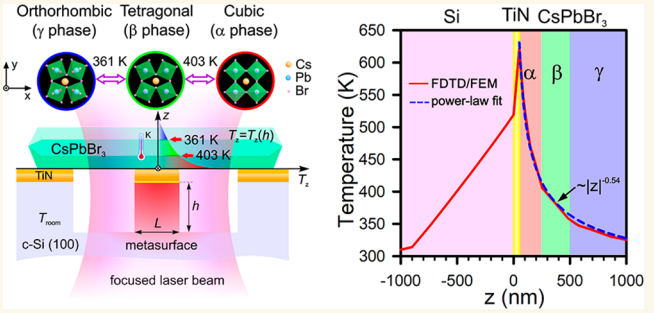

KEYWORDS: *halide perovskite, thermoplasmonics, metasurface, optical heating, phase transition, twin domains*

1. INTRODUCTION

Perovskite-structured direct-band-gap semiconductors form an important class of materials with equally important applications. The presence of antibonding states near the maximum of the valence band gives rise to a defect-tolerant semiconductor material with distinctive electronic and optical properties, including fast charge transport, an extended free carrier diffusion length, a high exciton binding energy, and band-gap tunability.[1−6] These properties have already enabled promising applications in photovoltaics and solar energy conversion with >20% efficiency,[7] as well as lasing and light-emitting devices.[3,4,6,8]

The properties of perovskite derive from its specific ABX_3 architecture, where A and B are cations and X are anions arranged into chemically stable corner-sharing octahedral BX_6 frameworks. There are three main crystallographic phases in which perovskites exist: namely, orthorhombic (γ), tetragonal (β), and cubic (α). Transitions among the aforementioned phases contribute to the formation of multiple structural domains and lattice imperfections, specifically through crystal twinning. This latter process can be understood as an immunity response to the loss of symmetry when, upon minimizing the Gibbs free energy, the system relaxes into a thermodynamically stable state by forming ferroelastic, near-orthogonal domains. These formations have been widely studied at the nano-, micro-, and mesoscales.[9−13] In perovskites, crystal twinning is associated with lowering of the lattice symmetry by tilting and contortion of octahedra, which causes spontaneous intrinsic stress. The introduction of such structural distortions will significantly affect the local electronic structure and hence transition probabilities. Moreover, the density of states is considerably greater at these sites, where the latter can be viewed as an optical nanoantenna.[14]

Temperature[15,16] and pressure[17] perturbations have been utilized to alter the system's properties through manipulation of the crystal structure and defect density. For many perovskite systems, the band gap for the tetragonal phase is slightly lower

Received: January 13, 2023
Accepted: March 24, 2023
Published: March 28, 2023

https://doi.org/10.1021/acsnano.3c00373
ACS Nano 2023, 17, 9235−9244

compared to those of the orthorhombic and cubic phases.[18,19] This causes free carriers to migrate from high- to low-band-gap areas, an effect that is most pronounced near phase transition sites. It has been hypothesized that such spatially nonuniform transport leads to a local buildup of free carriers in tetragonal domains.[20,21] Such an accumulation of free carriers increases the probability for electrons and holes to radiatively recombine, affecting and ultimately improving optical transitions near the lattice distortions sites. *If temporally and spatially controlled, this effect could be used to actively tune the optoelectronic properties of the material, such as boosting the brightness of light-emitting devices*[1,3] *or modulating the lasing efficiency.*[22,23] Control of such enhanced emission requires precise manipulation of phase structuring within the single crystal. This manipulation, in turn, necessitates control of the phase transitions and thus dynamic management of the local temperature within the material.

There are two major prerequisites for producing multiphase structures in a dynamically controlled manner: (1) a mechanism for rapid and efficient heating at the nano- to microscales and (2) a mechanism for heat release from the heated location. In this context, the heating mechanism at small spatial scales can benefit from the thermoplasmonic effect, through which heat can be locally generated via absorption of incident light by a plasmonically resonant structure.[24−26] This approach has been shown to be useful for efficient heat generation (up to a few thousands of K), followed by a rapid directional heat transfer to the material of interest.[26,27] Note that all-inorganic halide perovskites have notably small thermal conductivity (0.42 W m^{-1} K^{-1})[28] yet possess high light and thermal stability. The latter underlines the possibility of maintaining spatial and temporal stability of the heat pattern and gradients across a single crystal, resulting in a stable multiphase semiconducting system.

In this work, we demonstrate controlled multiphase structuring of a single crystal of cesium lead bromine ($CsPbBr_3$). We achieve this level of control by placing the perovskite crystal on a thermoplasmonic metasurface that consists of a 2D array of stacked titanium nitride (TiN) plasmonic nanopads on top of silicon (Si) nanopillars (Figure 1a).[29] When it is irradiated with visible light at a wavelength resonant with the TiN structure, the plasmonic nanopad serves as an *optically switchable heater*, while the Si pillar provides a channel for heat dissipation. This geometry produces subwavelength thermal gradients across the perovskite microplate, triggering on-demand formation of stable phase domains within the original single crystal.

2. RESULTS AND DISCUSSION

2.1. Device Concept. The $CsPbBr_3$ perovskite undergoes two reversible phase transitions above room temperature. These are the orthorhombic-to-tetragonal (361 K) and the tetragonal-to-cubic (403 K) phase transitions as determined with fast scanning calorimetry (FSC, Figure S1 and Section 1 in the Supporting Information). As the rate of the temperature sweep increases, the data clearly show the lack of mirror symmetry between heating and cooling experiments. This observation points to defect-induced spatial heterogeneity within the crystal and reflects an imbalance in the potential energy barriers associated with the conversion of structure from lower to higher symmetries and *vice versa*. This makes the FSC method highly sensitive to the crystalline imperfection content and density.

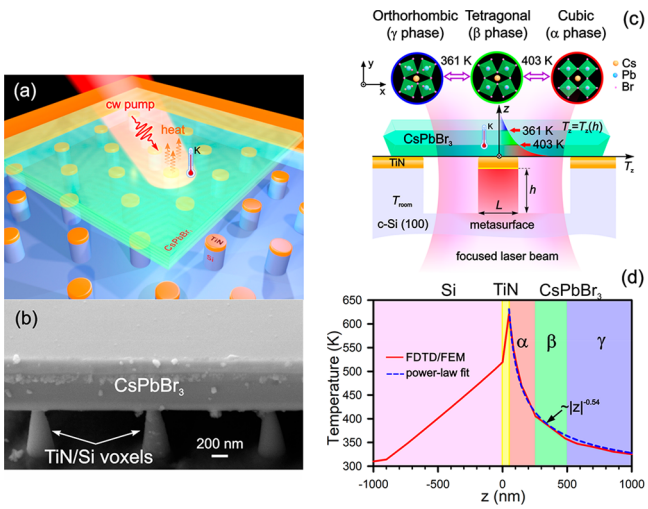

Figure 1. (a) Schematic representation of a $CsPbBr_3$ platelet mounted on a metasurface array. (b) A 72° tilted SEM image of the edge facet of the $CsPbBr_3$ platelet on the TiN metasurface. (c) Optical heating of halide perovskite crystal by the TiN/Si nanostructure. Color areas within the temperature gradient represent the *γ* phase of the *Pnma* space group (blue), the *β* phase of the *P4/mbm* space group (green) and the *α* phase of the *Pm3m* space group (red). (d) Finite-difference time-domain (FDTD) and finite element method (FEM) simulations of the axial temperature distribution across the TiN/Si and $CsPbBr_3$ crystal.

The presence of these phase transitions at high temperatures underlines the possibility to form a combination of different crystal phases in the material if steep and steady temperature gradients are introduced. Figure 1a schematically illustrates such a device concept that operates under ambient laboratory conditions. The $CsPbBr_3$ perovskite platelet (10 μm × 14 μm × 1 μm) is placed on a metasurface that is comprised of a hexagonal 2D array of Si pillars with a subwavelength base ($L < \lambda$). Each nanopillar is capped by a TiN plasmonic pad on top (Figure 1a,b). Upon illumination (continuous wave, 633 nm, 16 mW, 0.6 μm spot size, NA = 0.7), the TiN pad functions as a photothermal heater, while the Si pillar transfers heat down to the bulk substrate. Silicon was chosen as the thermostat material because of its large thermal conductivity (148 W m^{-1} K^{-1}) and strong Raman response (Si−Si 521 cm^{-1}). Moreover, its Raman activity is temperature sensitive, permitting its use as a probe for Raman-based thermometry.

The light-to-heat conversion is expected to be maximum at the plasmonic absorption resonance of the TiN structure, as characterized by the absorption power $P = \sigma_{abs} I_0$, where σ_{abs} is the absorption cross section and I_0 is the incident intensity.[24,25] The accessible temperature range at a thermal stationary state of the system will depend on several factors: namely, the effective thermal conductivity of Si, the pillar's lateral and axial dimensions, the permittivity ε of the TiN pad, and the incident flux I_0. The pillar geometry, defined by base lateral size L and height h, governs the heat dissipation efficiency, and its effect has been discussed previously for composite TiN/Si rods,[29−31] tubes, and trenches.[32] Taking into account the Fröhlich resonance condition, we can derive the temperature change from the ambient values at the top of the Si pillar as a function of structure height h and incident light intensity I_0 as[29,31]

https://doi.org/10.1021/acsnano.3c00373
ACS Nano 2023, 17, 9235−9244

$$\varepsilon'_{\mathrm{TiN}}(\lambda_0) = -2\varepsilon_{\mathrm{Si}}$$

$$\Delta T(h, I_0) \approx \frac{3}{4}\frac{L^2Q^2}{\beta\lambda_0}\varepsilon''_{\mathrm{TiN}}\left[\frac{1}{\kappa_{\mathrm{Si}}}I_0 - \frac{\sigma_{\mathrm{abs}}}{\kappa_{\mathrm{Si}}^3}\frac{\partial\kappa_{\mathrm{Si}}}{\partial T}hI_0^2\right] \quad (1)$$

where λ_0 is the wavelength at the plasmonic resonance, $\varepsilon = \varepsilon'_{\mathrm{TiN}} + i\varepsilon''_{\mathrm{TiN}}$ is the complex permittivity of a TiN heater, $Q = -\varepsilon'_{\mathrm{TiN}}/\varepsilon''_{\mathrm{TiN}}$ is a Q factor for the plasmon resonance, κ_{Si} is the temperature-dependent thermal conductivity of bulk Si, and β is the geometry-dependent dimensionless thermal capacity of TiN.[25] For smaller pillar heights (<200 nm), the first term dominates and ΔT is expected to show a linear dependence on I_0 (see Figure S2 in the Supporting Information).[29] For taller pillars, the contribution of the second term increases accordingly, resulting in a quadratic dependence of the temperature on I_0. Moreover, ΔT is now dependent on the first temperature derivative of κ_{Si}. For bulk Si, this derivative has a negative sign above room temperature, and thus, ΔT should monotonically increase with the incident intensity. For structures with height exceeding h > 500 nm, significant deviations from experimental observations have been reported and explained in terms of thermal anisotropy.[32]

Because the thermal conductivity of Si (κ_{Si} = 148 W m^{-1} K^{-1}) significantly exceeds that of both air (κ_{air} = 0.0263 W m^{-1} K^{-1}) and $CsPbBr_3$ perovskite (κ_{CsPbBr_3} = 0.42 W m^{-1} K^{-1}), the pillar structure becomes the dominant channel for heat dissipation, with its geometry being the key factor in determining the steady-state temperature profile. *Hence, pillars of a specific height provide access to specific temperature ranges, while fine control within this range can be realized by varying the incident light intensity I_0. On irradiation, an array of such nanoheaters can generate a two-dimensional temperature pattern formed by subwavelength hot spots ($L < \lambda$).*

Induced thermal gradients along the axial direction in the perovskite allow particular phase domains to be formed, subject to the distance from the heating TiN pad (Figure 1c). Figure 1d shows a combined finite-difference time-domain (FDTD) and finite element (FEM) method (ANSYS/Lumerical) simulation of the axial temperature distribution. The simulation reveals the axial heat distribution within the layered system, comprised of a 1 μm Si pillar, a 50 nm TiN pad, and a 1 μm $CsPbBr_3$ crystal. A pillar of this height is associated with a steady-state temperature range of 320−520 K or a 0.23 K/nm thermal gradient within the Si material. The maximum temperature at the plasmonic structure is chosen to be 630 K, a critical temperature point beyond which the $CsPbBr_3$ optoelectronic properties drastically change.[33] The temperature gradient in the perovskite interior follows a $|z|^{-0.54}$ dependence, found from least-squares fitting (R^2 = 0.997), which is mainly determined by crystal thermal conductivity. In these simulations, the surrounding medium is assumed to be air. Depending on the initial nanopad temperature (i.e., input light flux), the crystal interior can be comprised of a single γ phase or a structure of two or all three phases, as shown for T_0 = 630 K in Figure 1c.

2.2. Optical Visualization of Phase Transitions and Crystal Twinning. The real time dynamics of domain formation and twinning in perovskite crystal on a microscale is shown in Movie SM1 in the Supporting Information. In this experiment, the crystal was placed on a hot plate to perform temperature sweeps from 340 to 410 K and back, spanning the orthorhombic-to-tetragonal-to-cubic phase transitions. The heating and cooling rates were sufficiently slow to allow a uniform temperature to establish itself throughout the crystal. Optical imaging and other spectroscopic experiments were performed with the aid of a sample piezo positioning feedback system, as described in Section 3 of the Supporting Information. This solution overcomes experimental obstacles such as the thermal expansion of the sample and setup elements. It also corrects for beam defocusing by the Bragg-like grating formed through crystal twinning within the sample volume (see Methods and Figure S3 and Section 3 in the Supporting Information).

Figure 2 depicts confocal reflection images of the crystal surface at selected steady-state temperatures. At 303 K (Figure 2a), the crystal consists of parallel domains of the γ phase that are oriented at a 45° angle (⟨110⟩) relative to the lab frame. The transition to the tetragonal phase occurs at around 393 K (Figure 2b). As the temperature is increased to 408 K, the stripes disappear completely, indicating the formation of a homogeneous cubic crystal (α phase, Figure 2c). As the system cools down and crosses the cubic-to-tetragonal transition, crystal twinning triggers the formation of multiple tetragonal domains (Figure 2d) and a further temperature decrease brings the crystal back into the orthorhombic phase (Figure 2e). The data show clear differences between the images of the crystal at the same temperature points but opposite ends of the temperature cycle (Figure 2a,e).

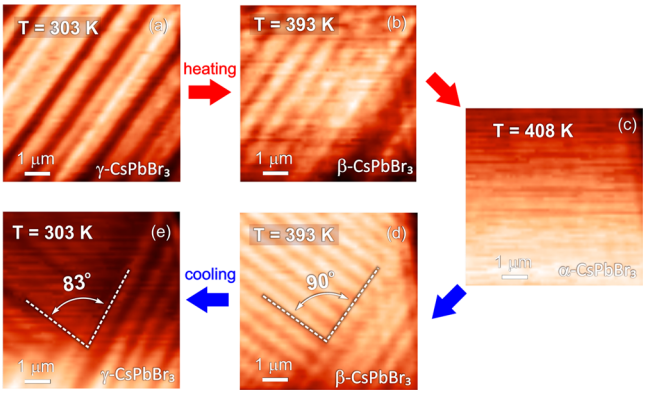

Figure 2. Confocal reflection images of a $CsPbBr_3$ crystal using polarized light at (a) 303 K (orthorhombic phase), (b) 393 K (tetragonal phase), and (c) 408 K (cubic phase) and back to (d) 393 K (tetragonal phase) and (e) 303 K (orthorhombic phase).

This difference in the patterns further confirms the results of the FSC experiments (Figure S2), indicating that the potential energy barriers are different when the phase transition proceeds along different directions of the temperature sweep. *The symmetries of the original and final crystallographic phases associated with a transition are the key factors in the evolution of the crystal twinning.* Upon careful examination, it is clear that the resultant orthorhombic phase reveals a 7° deviation angle relative to the previously orthogonal orientation of the domains in the tetragonal phase (Figure 2d,e). This is in excellent agreement with previous calculations by density functional theory (DFT) that yielded a $\phi \approx 13°$ octahedral tilt for orthorhombic $CsPbBr_3$.[18] The rotation of the corner-sharing Br atoms of the $[PbBr_6]^{4-}$ octahedron in the equatorial plane by $\phi/2 \approx 6.5°$ should result in a relative reorientation of the domains to $90° - \phi/2 \approx 83.5°$, as demonstrated in Figure 3f.

https://doi.org/10.1021/acsnano.3c00373
ACS Nano 2023, 17, 9235−9244

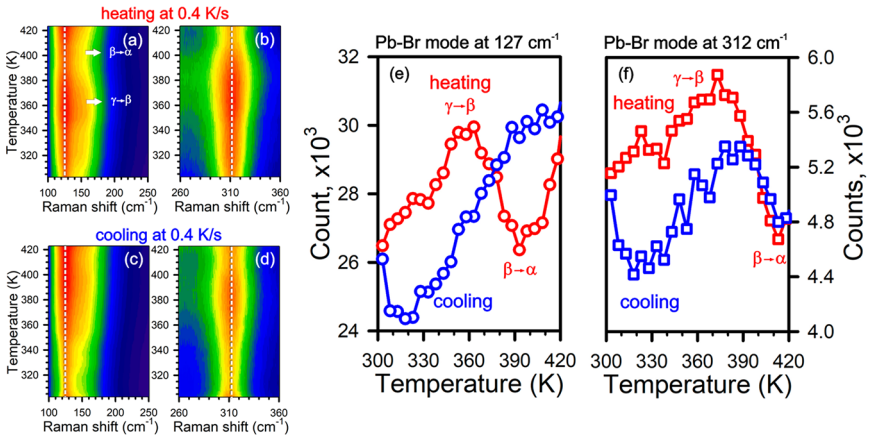

Figure 3. Temperature-dependent Raman spectroscopy of a $CsPbBr_3$ crystal at thermal equilibrium for the TO phonon mode at 127 cm^{-1} (a, c) and LO two-phonon mode at 312 cm^{-1} (b, d) upon heating and cooling at a rate of 0.4 K/s. (e, f) Cross sections at the peak center for TO and 2LO modes (dashed lines in (a–d).

2.3. Temperature Dependence of Raman and Photoluminescence Signatures. Both the FSC and the optical imaging experiments reveal information about the phase transitions in the perovskite crystal, and both measurements point to the importance of lattice imperfections and distortions. To examine their role at the microscopic level, we performed Raman and photoluminescence experiments, which are particularly sensitive to the electronic structure near defects and phase interfaces.

The Raman spectrum of $CsPbBr_3$ perovskite features two main low-energy vibrational modes: namely, the 127 cm^{-1} TO (first-order transverse optical) and the 312 cm^{-1} 2LO (second-order longitudinal optical) Pb–Br stretching phonon modes (Figure 3a–d).[34] It is important to note that the presence of the 312 cm^{-1} peak in the Raman spectrum is evidence for the more pristine $CsPbBr_3$ structure relative to the presence of $CsPb_2Br_5$, with the latter being the result of exposure to water.[35]

The temperature dependences of the Raman spectra for both the TO and 2LO modes are different for various directions of the temperature sweep (Figure 3e,f) of a uniformly heated crystal. As the temperature is increased, the intensity of the TO phonon line (127 cm^{-1}) undergoes two extrema corresponding to the orthorhombic-to-tetragonal (361 K) and tetragonal-to-cubic (403 K) phase transitions (Figure 3a,e). The β-$CsPbBr_3$ phase reveals an expected trend, namely the decrease of the Stokes intensity with temperature, caused by the band-gap contraction and the depletion of carriers in the valence band.[18,19] Meanwhile, the temperature dependence of the Stokes bands ascribed to the α and γ phases shows the opposite trend (Figure 3e). This observation can be explained by the interplay between the thermal volumetric expansion and the tilt of the $[PbBr_6]^{4-}$ octahedra.[18] It has been predicted that both mechanisms are capable of significant widening of the band gap,[19] estimated to be <2.0 eV for β-$CsPbBr_3$ versus ~2.36 eV for γ-$CsPbBr_3$ and ~2.4 eV for α-$CsPbBr_3$. These band-gap variations offer possible explanations for the observed positive temperature trends. For example, for the given experiments the Raman process in the β-phase is closer to the resonance for the excitation photon energy used (633 nm, 1.96 eV). This may lead to a signal increase when more β-phase sites are introduced. Another potential mechanism deriving from the contribution of the shallow and deep states to the free carrier population at the conduction band is expected to increase with temperature,[36] enabling a change in the Raman polarizability.[37]

When the temperature is lowered, the Raman intensity of the TO mode decreases continuously to 315 K, at which a minimum is observed. We speculate that such behavior can be understood from the dominant role of the crystallographic deformation of the $[PbBr_6]^{4-}$ backbones with cooling. Spatially resolved Raman intensity maps for each phonon mode at different temperatures are presented in Figure S4. The images agree well with the confocal reflection images (Figure 2). They demonstrate a clear variation in the domain pattern as a function of the directionality of the temperature sweep across particular phase transitions—a result of the unequal potential energy barriers of the high-to-low and low-to-high symmetry conversions.

The difference in crystal twinning also impacts the temperature trend of the TO and 2LO phonon lines, resulting in their characteristically different behaviors (Figure 3e,f). For the TO phonon mode, electron–phonon scattering at the Γ point is more sensitive to twin domain formation due to the overall momentum restrictions for the one-phonon process. This is opposite for the 2LO mode, for which there is a simpler path to fulfill momentum conservation due to the involvement of two phonons to scatter light inelastically. While the 2LO line clearly shows the $\gamma \rightarrow \beta$ transition (red curve, Figure 3f), at the same time it appears insensitive to the $\beta \rightarrow \alpha$ transition. Likewise, the cooling curve exhibits the same local extrema features: namely, the 2LO mode is sensitive to the $\gamma \rightarrow \beta$ transition but not to the $\beta \rightarrow \alpha$ transition. Whereas the multiphonon mode can be utilized as a temperature probe for a defect-free crystal, the single-phonon TO mode is more sensitive to the orthorhombic-to-tetragonal and tetragonal-to-cubic phase transitions.

Photoluminescence (PL) microspectroscopy provides additional information on the carrier dynamics and the origin of the emission mechanism. The latter has been investigated through power dependence and fluorescence lifetime studies and is discussed in detail in Section 5 in the Supporting Information. Here, we focus primarily on the temperature trends of perovskite photoemission. When the temperature is raised, the PL intensity drops dramatically (Figure 4a), reaching a minimum at $T_{\gamma\rightarrow\beta}$ at 361 K. Further increase of the lattice temperature gives rise to a higher PL intensity for the tetragonal (β) and cubic (α) phases (red curve, Figure 4c).

https://doi.org/10.1021/acsnano.3c00373
ACS Nano 2023, 17, 9235–9244

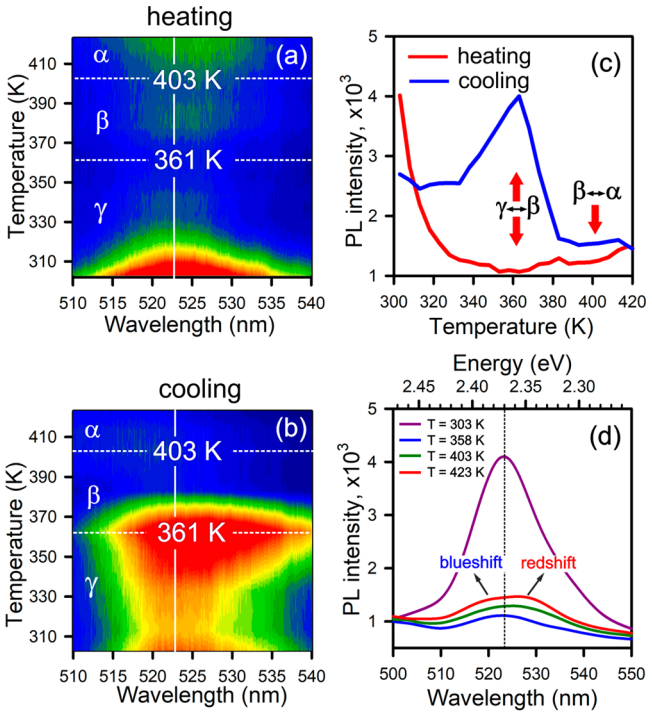

Figure 4. (a, b) False-color PL maps for different signs of temperature sweep. (c) Cross sections along the vertical dashed straight lines at the center of the PL spectrum. (d) PL spectra at different temperatures.

The overall PL spectral shape reveals complex behavior through the sweep, showing splitting-like behavior at high temperatures (Figure 4b). First, a blue shift of the mean of the spectral distribution (~16 meV) is observed (Figure 4d), indicating the band-gap expansion of the cubic phase at 423 K.[19,37] Second, a red-shifted signature (~18 meV) is observed, which is suggested to originate from the competition between surface and interior contributions of the crystals (Figure 4d).[37,38]

A radically different trend is observed when cooling is performed, with fluorescence showing a strong local maximum at the $\gamma \rightarrow \beta$ transition (Figure 4b,c). A similar observation has been reported for methylammonium lead triiodide ($CH_3NH_3PbI_3$ or $MAPbI_3$), upon cooling from 160 to 140 K.[20] The nature of the PL enhancement across this phase transition can be understood as resulting from the funneling effect,[20] when mobile carriers migrate to the "defect-free" low-band-gap tetragonal phase.

The observed hysteresis agrees well with the confocal reflection and Raman studies and can be understood in a similar manner—lattice reconstruction and the dependence of crystal twinning on the sign of the temperature change ΔT. Since twinning requires the base of one domain to be matched to and shared with the side of another, its probability will strongly depend on the presence of inherent crystal imperfections and the geometry of the original and resultant phases. This leads to significant differences in the overall pattern of the multidomain assembly as a function of the sign of the temperature trend and, in turn, the number of structural defects and phase interfaces being formed. This phenomenon also explains the striking contrast in the PL quantum efficiency. It suggests that the presence of point defects and crystal twinning favors the $\beta \rightarrow \gamma$ transition and hinders PL for the reverse direction of the transition.

2.4. Optical Properties of a Multiple-Phase Single Crystal. After the optical characterization of pervoskite platelets held at a uniform temperature, using reflection, Raman, and photoluminescene microspectroscopy, we next used these optical tools to study crystals subjected to a temperature gradient. For this purpose, we employed the metasurface heating device discussed in Section 2.1 to maintain stable temperature gradients in the crystal and control the distribution of phase domains in the axial (z) direction.

Figure 5a shows a scanning electron microscope (SEM) image of a $CsPbBr_3$ microplate placed on the metasurface. Figure 5b1–b3 (cyan, yellow, and magenta) depicts 72, 48, and 48° tilted images of the corners marked with an arrow of the corresponding color (Figure 5a), respectively. As is clear from the images, the structure is formed by two stacked crystal plates, most clearly observed through their exfoliation at one of the corners (Figure 5b1 and Figure S6 in the Supporting Information). The metasurface is comprised of a 2D hexagonal array of TiN/Si voxels with a pillar height estimated to be approximately 900 nm, as shown in Figure S7 in the Supporting Information. The top of the voxel is visualized in the inset of Figure 5a. It is clear that, upon illumination, the TiN pads become damaged for intensities exceeding 3 MW/cm^2 (green and blue contoured images in the inset of Figure 5a).

The confocal reflection image at 633 nm of the perovskite platelet is shown in Figure 5c. In this image, the uncovered TiN/Si voxels have been placed at the focal plane of the objective. For such an arrangement, the voxels that are covered by the perovskite appear out of focus, as light has to penetrate through the 1 μm thick material of refractive index n = 2.5.[37] This effect not only prevents efficient heating of the TiN pads but also limits the efficient collection of the Raman signal from the voxel. The collection efficiency is instrumental, as the Raman response was utilized as a remote temperature probe. In all further experiments, the light was focused on the top of the TiN/Si voxels that are under the $CsPbBr_3$ microplate.

Figure 5d displays the results of confocal PL imaging. PL spectra as a function of spectral position on the sample were collected using 1.7 W cm^{-2} of 473 nm excitation. It is important to note that such low fluxes did not introduce any meaningful temperature gradients. In addition, the excitation wavelength used is far away from the absorption resonance of the plasmonic structures. The false-color PL map can be divided into three characteristic regions according to PL spectral shape and central frequency position (Figure 5e)—blue (522 nm, 2.375 eV), red (531 nm, 2.335 eV), and an intermediate green region. We observe a clear correlation between the PL spectrum and the sample thickness and/or stacking. Higher energy PL, centered around 522 nm (2.375 eV), is observed in areas where two thin ~400 nm plates are stacked (blue spot in Figure 5d,b2).

However, the spectrum is red-shifted by 40 meV at the position where the sample appears to consist of a 1 μm thick single plate (red spot in Figure 5d,b3). It has been suggested that the observed phenomenon is caused by the excitation of waveguide modes within the Fabry–Perot resonator through the absorption–emission–absorption mechanism.[34] If true, monitoring of the PL spectral position offers a means to probe the distribution of the perovskite thickness.

https://doi.org/10.1021/acsnano.3c00373
ACS Nano 2023, 17, 9235–9244

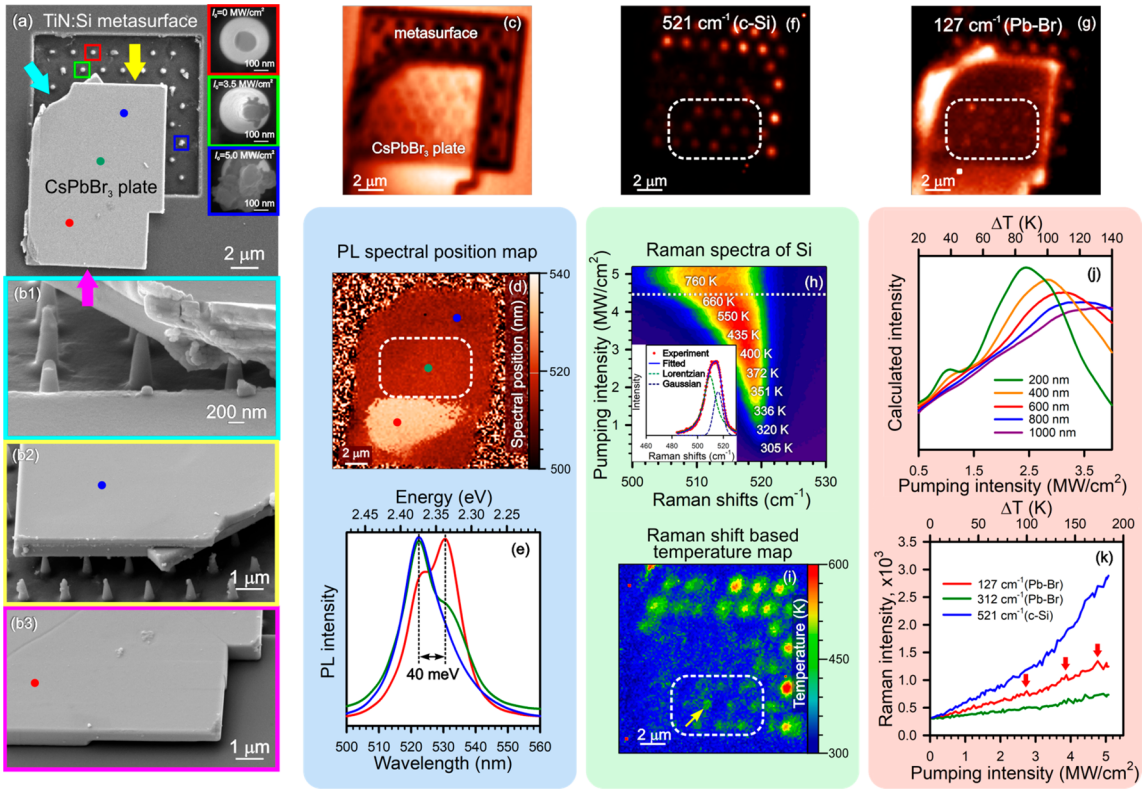

Figure 5. $CsPbBr_3$ platelet on the thermoplasmonic TiN/Si metasurface. (a) SEM image of the $CsPbBr_3$ plate over the metasurface. The insets show TiN/Si voxels, marked with red, green, and blue squares, exposed to 633 nm cw illumination with intensity of 0, 3.5, and 5.0 MW/cm^2, respectively. (b1−b3) SEM images (side views at the tilt angles of 72° (b1) and 48° (b2, b3) from the sides marked with cyan, yellow, and magenta arrows in (a). (c) Confocal reflection image at 633 nm. (d) False-color PL spectrum central frequency map. (e) PL spectra taken at spots marked in (d) with red, blue, and green filled circles, respectively. (f, g) Raman maps at 521 cm^{-1} (c-Si) and 127 cm^{-1} (Pb−Br mode). (h) Raman spectra of a Si pillar as a function of input light intensity. The inset shows a cross section along a dashed white line and numerical deconvolution of the composite band into Lorentzian and Gaussian components. (i) Temperature map measured based on Raman thermometry. (j) Simulated cumulative Raman signal from phase-structured crystals of different thicknesses. (k) Raman intensity vs the pumping intensity or gradient initial temperature T_0 for 127 cm^{-1} (green) and 312 cm^{-1} (red) of perovskite phonon modes and 521 cm^{-1} Si line.

Figure 5f,g shows confocal Raman maps for the 521 cm^{-1} (c-Si peak of the pillar) and 127 cm^{-1} (TO Pb−Br phonon mode of $CsPbBr_3$) lines, respectively. It is evident that not all voxels under the platelet can be clearly differentiated in the image. This is caused by the damage while positioning the perovskite on the metasurface and/or by the poor contact at certain positions. An array of proper spots above the damage-free Si pillars is outlined with a dashed loop (see Figure 5f,g,d,i). The enhanced Raman scattering of the TO mode at the crystal edges originates from structural inhomogeneities, where the density of surface states is higher (Figure 5g). For quantitative monitoring and visualization of the temperature at the voxel, we used Raman thermometry. This method, thoroughly described elsewhere[29−31] (see Section 8 in the Supporting Information), utilizes the temperature-dependent behavior of the c-Si Raman signal (521 cm^{-1}) as a remote probe. Through the use of an Echelle grating, the spectral resolution of the imaging system reaches 0.1 cm^{-1} and enables temperature measurements with 5 K accuracy. Figure 5i shows a Raman-shift-based temperature map of the metasurface capped with a $CsPbBr_3$ crystal. For further analysis the most bright voxel beneath the perovskite plate, marked with an arrow, will be utilized.

A detailed analysis of the open voxel temperature (blue voxel, Figure 5a) versus input flux is shown in Figure 5h. Note that the c-Si mode is asymmetrically broadened (inset, Figure 5h). This effect originates from the nonuniform heat distribution in the structure, resulting in the presence of contributions from both hot and cold portions of the material.[31] To further simplify the analysis, the spectrum was fitted with Lorentzian (hot medium contribution) and Gaussian (cold medium contribution) spectral line shapes, using a regularized least-squares method (R^2 = 0.998). The intensity map in Figure 5h clearly indicates that the contribution from hot domains deviates significantly from a linear incident intensity dependence for intensities exceeding 4 MW cm^{-2} (550 K). We attribute this effect to temperature-dependent changes in the TiN permittivity, which affects the plasmon resonance frequency. In addition, the thermal conductivity of Si decreases when the temperature is raised.[39]

The signs of degradation of the TiN pad appear at 750 K, where the Raman intensity peaks at about 5 MW cm^{-2} and then shifts back to the higher-energy side. This is also confirmed by previous experiments using ellipsometry on TiN films.[29] Thus, in our experiments, the incident light flux enabled access to the 293−473 K temperature range—sufficient to activate all necessary structural transitions in $CsPbBr_3$ while preventing photodamage of the plasmonic structures. Figure 5h shows the resulting temperature map

https://doi.org/10.1021/acsnano.3c00373
ACS Nano 2023, 17, 9235−9244

derived from the Raman shift using eq S1 (see Figure S9) and measured at 3.5 MW cm^{-2}.

The local generation of hot spots produced thermal gradients throughout the perovskite crystal. This effect resulted in the simultaneous formation of multiple phase domains, as illustrated in Figure 1. However, there are significant and fundamental differences between the temperature trends of the Raman signals when (1) heating of the whole crystal by a hot plate to achieve a uniform temperature profile, as opposed to (2) establishing a temperature gradient in the crystal with the metasurface. For the first case, the upward temperature trend discussed in Section 2.3 is shown by the red curve in Figure 3e. This profile shows clear extrema at phase transitions with an overall signal intensity decrease across the tetragonal phase. In the second case, when the crystal is locally heated by the plasmonic structures, the temperature gradient induces multiple phases in the axial direction. For this case, *the Raman response is the cumulative signal from all the phases in the collection volume*.

The trend of the cumulative Raman signal I_R versus the plasmonic pad temperature $T_m(0)$ should directly reflect the process of multiphase structuring of the perovskite. The trend can be modeled as discussed in Section 10 in the Supporting Information. For simplicity, one can assume one-dimensional heat dissipation in a homogeneous perovskite crystal, in which the temperature profile obeys a $T_m(z) = T_m(0)|z|^{-0.54}$ power law in the axial direction (Figure S10). The resulting Raman response can then be written as

$$I_R = \int_0^{\Delta z} \langle I(z) \rangle \, dz \tag{2}$$

where $\langle I(z) \rangle$ is the average Raman signal of the homogeneous media at a given z plane (Figure S10) and Δz is the total crystal thickness. Figure 5j shows plots of I_R vs I_0 for different Δz values of perovskite. As expected, for very thin crystals (<200 nm), the temperature trend of Raman signal closely follows that previously observed for a thermally equilibrated crystal on a hot plate (green curve Figure 5j, red curve Figure 3e). For thicker crystals, multiple phases can contribute to the observed Raman signal. The local maximum remains highly pronounced over the monotonically increasing Raman response, indicating the formation and growth of a two-phase structure (γ and β) in the axial direction.

This model agrees well with experimental observations. Figure 5k shows the intensity evolution of the phonon modes (TO 127 cm^{-1}, 2LO 312 cm^{-1}) along with the c-Si line (521 cm^{-1}) as a function of the incident light flux/pad temperature. As expected, the trends for the 127 cm^{-1} (Pb−Br) and 312 cm^{-1} (Pb−Br) modes are inherently different from the case of the thermally equilibrated system (red and green curves, Figure 5k). For the TO mode, a clear presence of local maximum around the temperature of the γ-to-β transition is observed, indicating the formation of a two-phase structure. Upon further increase of the pad temperature $T_m(0)$, another shallow bump at $\Delta T \approx 140$ K indicates triple-phase formation (α, β, and γ).

To visually emphasize these signatures, the linear contribution to the Raman-temperature trend has been subtracted in Figure 6a. The linear contribution has been determined from a simple linear fit over the 0−2.5 MW cm^{-2} range (Figure 6a, point b, and Figure 6b), where the whole perovskite crystal remains in the single orthogonal γ phase and the intensity of the TO Raman peak should linearly increase with the incident excitation flux and temperature (Figure 3e). Upon increasing

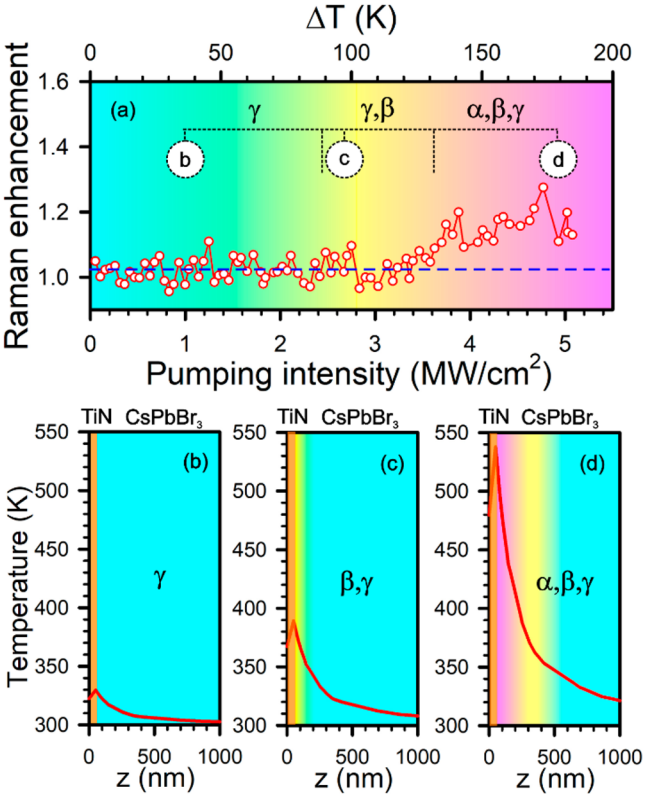

Figure 6. (a) Linearly corrected Raman response versus the incident light flux. (b−d) Simulated temperature points where single-, double-, and triple-phase structures occur as seen in Raman signatures from (a). The blue dashed line represents the subtracted linear contribution.

the incident intensity, the formation of the tetragonal phase at the interface of the perovskite and TiN is expected to occur at point c (Figure 6a). At this point of the trend, the steep temperature gradient creates a spatially sharp defect area where the crystal is in a transitional form between the orthorhombic and tetragonal phases (Figure 6c). This scenario manifests itself as a shallow Raman intensity maximum. Further increase of the plasmonic pad temperature drives the β-phase deeper into the crystal bulk. At $\Delta T \approx 130$ K another shallow maximum of the TO Raman peak indicates the formation of the α-phase in close proximity to the TiN structure. Upon subsequent increase of the incident light flux, the α and β phases extend further into the crystal and significantly broaden (Figure 6d). This is expected to result in the smearing of the boundaries between the different phases. This effect is spatially asymmetric, i.e. different for the left (α−β) and the right (β−γ) sides of the β phase, following the highly nonlinear temperature gradient. At higher temperatures, the signal is an interplay of several contributions, in particular the phase layer thickness, the temperature, the position along the gradient, and the sharpness of the phase boundary. We hypothesize that the third maximum at $\Delta T = 170$ K is the result of such a cumulative effect and may be associated with the delocalized (disordered or randomly located) phase boundary. Among other instrumental contributors to the spatial phase formation are the crystal intrinsic defects. Their presence can trigger the spontaneous formation of different phases, resulting in a highly irregular structural front. At higher TiN temperatures, the α−β and β−γ boundaries broaden significantly and may capture

https://doi.org/10.1021/acsnano.3c00373
ACS Nano 2023, 17, 9235−9244

more defects into these areas where the phases are highly mixed.

These experiments demonstrate that the Raman signal from a perovskite subjected to a stable temperature gradient, as shown in Figure 5k and emphasized in Figure 6, reveals distinct behavior that is in contrast to a bulk crystal held at uniform temperature. The dependence of the Raman signal on the incident intensity shows clear signatures of particular phase formations, their extension into the bulk of the material, and, overall, the multiphase structuring process (see Section 10 in the Supporting Information for a complete statistical analysis of the data). Moreover, it shows that the detected Raman signal exhibits notable gain across ΔT = 150 K. Using Raman microspectroscopy as a probe, these results indicate that it is possible to generate on demand a distribution of single-, double-, and triple-phase structures in perovskite by simply controlling the incident light intensity.

3. CONCLUSIONS

In this work, we have demonstrated a proof-of-principle multiphase structured single crystal $CsPbBr_3$ halide perovskite. We have shown that the single-, double-, and triple-phase systems can be created in an optically controlled fashion on the thermoplasmonic metasurface using the continuous wave illumination of modest intensities. Light-induced heat from plasmonic TiN nanopads forms strong temperature gradients within the crystal bulk that are followed by a sequence of corresponding phase transitions.

Lattice distortions, defects, and impurities operate like an optical nanoantenna, increasing the density of states. Thus, multiphase perovskite structures have many interesting properties. In such a system, charge carriers migrate from a lower symmetry lattice with large band gap (orthorhombic and cubic) to higher symmetry, but lower band gap, crystal parts (tetragonal). There, highly concentrated and in close proximity to the boundaries, carriers efficiently recombine, leading to areas with significant enhancement of the optical emission. This multistructured system promises to be highly beneficial to the development of next-generation ultracompact broad-band light-emitting diodes showing high PL quantum yields above room temperatures.

4. METHODS

4.1. Synthesis of $CsPbBr_3$ Structures. Perovskite microcrystals on glass substrates were synthesized by using a protocol similar to that previously reported.[40] $PbBr_2$ (110 mg) and CsBr (62 mg) were mixed and dissolved in 3 mL of anhydrous dimethyl sulfoxide (DMSO) inside a nitrogen-filled glovebox. A droplet of the prepared solution (volume 2 μL) was drop-casted on the substrate under ambient conditions. After that, the substrate was sealed in a Petri dish preheated to 60 °C containing 200 μL of the liquid mixture. The solution was dried in the presence of azeotropic vapor for 5 min. As a result, randomly oriented separate $CsPbBr_3$ microcrystals were formed on the substrate.

4.2. Synthesis, Nanofabrication, and Characterization of a TiN/Si Metasurface. TiN thin films on c-Si (100) substrates were DC magnetron sputtered from a Ti target in an Ar/N_2 environment with a volume proportion of 30:70 at an elevated temperature of 350 °C, a base pressure of 3×10^{-9} mbar, and a power of 200 W. Prior to the film growth, the c-Si substrate was sonicated in acetone for 15 min. The thickness of the TiN films, equal to 50 ± 5 nm, was measured with a Alpha Step 200 contact profilometer.

A 2D array of TiN/Si voxels was engraved with the help of focused ion beam (FIB) milling at a lower current of 1 pA by using a Quanta 3D FEG instrument (FEI). Since the higher TiN/Si voxels are exposed to FIB for a longer time, their lateral size is reduced due to edge melting. To avoid this detrimental effect, we used different mask templates for short and long voxels so that their lateral size was the same regardless of height.

The temperature-dependent permittivities of TiN thin films were measured with a spectroscopic ellipsometer (VASE, J. A. Woollam) within the spectral range of 250−2500 nm. The incident angle was 70°. The TiN sample was exposed to thermal annealing at the fixed temperature, whereas its permittivity was probed at room temperature. The temperature increment for each subsequent cycle was 100 °C. The temperature ranged from 25 to 600 °C. The samples were annealed in ambient air for 30 min using a heating stage (Linkam Scientific Model THMS600). The heating and cooling rates were 150 and 100 °C/min, respectively.

4.3. Fast Scanning Calorimetry. The fast scanning calorimetry (FSC) curves were registered on a FlashDSC2+ instrument (Mettler-Toledo, Greifensee, Switzerland) equipped with a TC100MT intracooler with a UFH1 sensor. The temperature calibration was performed using biphenyl (T_m = 69.2 °C) and benzoic acid (T_m = 122.3 °C) as standards to ±1 °C.

A single perovskite crystal was placed in the center of the calorimetric sensor. To improve the signal-to-noise ratio, the crystal size was chosen such as to almost match the active area of the sensor. Within the temperature range from 20 to 180 °C the sample was chemically stable, and the curves were repeatable, which allowed for averaging multiple scans to further improve the signal-to-noise ratio.

4.4. Atomic Force Microscopy. An NTEGRA PRIMA (NT-MDT) multimode scanning probe microscope was utilized for visualizing the topography of the $CsPbBr_3$ microplate surface and the thermoplasmonic metasurface. The AFM probes of the "VIT_P" series with resonant frequencies around 350 kHz were used in AFM measurements. The $CsPbBr_3$ microplate mounted on the metasurface fabricated by focused ion beam milling was measured in tapping mode with a free amplitude A_0 of 10−20 nm and a set-point value of $A_0/2$.

4.5. Far- and Near-Field Raman Spectroscopy and Microscopy. Raman spectra and maps were captured with an NTEGRA SPECTRA (NT-MDT) multipurpose analytical instrument in an inverted configuration. The confocal spectrometer was wavelength calibrated with a crystalline silicon (100) wafer by registering the first-order Raman band at 521 cm^{-1}. The sensitivity of the spectrometer was as high as ca. 3000 photon counts per 0.1 s, provided that we used a 100× objective (NA = 0.7), an exit slit (pinhole) of 100 μm, linearly polarized light with a wavelength of 632.8 nm, and power at the sample of 16 mW. No signal amplification regimes of a Newton EMCCD camera (ANDOR) were used.

128 × 128 pixel Raman maps were raster scanned with an exposure time per pixel of 0.1 s and were finally collected with the EMCCD camera cooled to −95 °C. Raman spectra within the range of from −2000 to +2000 cm^{-1} were registered with a spectral resolution of 0.1 cm^{-1} using an Echelle grating.

4.6. Fluorescence Lifetime Imaging Microscopy. To measure the PL decay time, we used a confocal optical spectrometer (NTEGRA SPECTRA) that includes a picosecond diode laser (BDL-SMN) generating pulses of 473 nm wavelength, 30 ps pulse duration, and 80, 50, or 20 MHz repetition rate, a Simple-Tau 150 TCSPC FLIM module (Becker&Hickl), and a HPM-100-40 GaAsP hybrid detector (Becker&Hickl). The detector has a detection efficiency of about 50% and is free of afterpulsing.

4.7. FDTD/FEM Calculations. 3D simulation of optical absorption of a TiN/Si voxels consisting of stacked TiN and Si cylinders under cw illumination was performed by using an Ansys/Lumerical FDTD solver. The height of the TiN pad was 50 nm, whereas the height of the Si pillar was 900 nm. To avoid anomalous electric fields near the TiN pad edge, we used disks with rounded edges (10 nm rounding). A mesh overlayer of 1 nm was utilized around the TiN pad and a rougher 10 nm mesh for the rest of the structure. Perfectly matching layers were used as boundary conditions for three directions. The optical and thermal properties of Si and air were imported from the Ansys/Lumerical material database. The TiN pad was exposed to a 632.8 nm focused laser light (NA = 0.7) with an

https://doi.org/10.1021/acsnano.3c00373
ACS Nano 2023, 17, 9235−9244

intensity of 5 MW/cm^2. The temperature profile was calculated through an Ansys/Lumerical FEM solver in the steady-state regime. The thermal conductivity of all constituents was assumed to be temperature-independent. The boundary condition of T = 300 K was set at z_{min} = −20000 nm of the 20 × 20 × 5 μm^3 simulation region.

ASSOCIATED CONTENT

Supporting Information

The Supporting Information is available free of charge at https://pubs.acs.org/doi/10.1021/acsnano.3c00373.

Details of the Raman thermometry approach, SEM, AFM, and confocal microscopy data, theoretical model of phase-gradient formation, and analysis of temperature-dependent Raman scattering from the multiphase structure (PDF)

Movie showing the wide-field visualization of real-time dynamics of phase transitions and crystal twinning in a perovskite crystal (MP4)

AUTHOR INFORMATION

Corresponding Authors

Sergey S. Kharintsev − *Department of Optics and Nanophotonics, Institute of Physics, Kazan Federal University, Kazan 420008, Russia;* orcid.org/0000-0002-5788-3401; Email: skharint@gmail.com

Dmitry A. Fishman − *Department of Chemistry, University of California, Irvine, California 92697, United States;* orcid.org/0000-0001-6287-2128; Email: dmitryf@uci.edu

Authors

Elina I. Battalova − *Department of Optics and Nanophotonics, Institute of Physics, Kazan Federal University, Kazan 420008, Russia*

Timur A. Mukhametzyanov − *Department of Physical Chemistry, Institute of Chemistry, Kazan Federal University, Kazan 420008, Russia*

Anatoly P. Pushkarev − *School of Physics and Engineering, ITMO University, St. Petersburg 197101, Russia;* orcid.org/0000-0002-1793-6812

Ivan G. Scheblykin − *Department of Chemistry, Lund University, 221 00 Lund, Sweden;* orcid.org/0000-0001-6059-4777

Sergey V. Makarov − *School of Physics and Engineering, ITMO University, St. Petersburg 197101, Russia; Qingdao Innovation and Development Center, Harbin Engineering University, Qingdao 266000 Shandong, People's Republic of China;* orcid.org/0000-0002-9257-6183

Eric O. Potma − *Department of Chemistry, University of California, Irvine, California 92697, United States;* orcid.org/0000-0003-3916-6131

Complete contact information is available at: https://pubs.acs.org/10.1021/acsnano.3c00373

Notes

The authors declare no competing financial interest.

ACKNOWLEDGMENTS

This work was supported by grant No. 19-12-00066-P of the RSF. The PL decay time measurements were granted by the Kazan Federal University Strategic Academic Leadership Program (PRIORITY-2030). The authors acknowledge technical support from our industrial partners: SCANSENS (GmbH, Germany) and NT-MDT BV (The Netherlands).

REFERENCES

(1) Dey, A.; Ye, J.; De, A.; Debroye, E.; Ha, S. K.; Bladt, E.; Kshirsagar, A. S.; Wang, Z.; Yin, J.; Wang, Y.; Quan, L. N.; Yan, F.; Gao, M.; Li, X.; Shamsi, J.; Debnath, T.; Cao, M.; Scheel, M. A.; Kumar, S.; Steele, J. A.; et al. State of the Art and Prospects for Halide Perovskite Nanocrystals. *ACS Nano* **2021**, *15*, 10775−10981.

(2) Ahmadi, M.; Wu, T.; Hu, B. A Review on Organic-Inorganic Halide Perovskite Photodetectors: Device Engineering and Fundamental Physics. *Adv. Mater.* **2017**, *29*, 1605242.

(3) Chen, J.; Xiang, H.; Wang, R.; Li, Y.; Shan, Q.; Xu, X.; Dong, Y.; Wei, C.; Zeng, H. Perovskite White Light Emitting Diodes: Progress, Challenges, and Opportunities. *ACS Nano* **2021**, *15*, 17150−17174.

(4) Kovalenko, M. V.; Protesescu, L.; Bodnarchuk, M. I. Properties and Potential Optoelectronic Applications of Lead Halide Perovskite Nanocrystals. *Science* **2017**, *358*, 745−750.

(5) Tailor, N. K.; Kar, S.; Mishra, P.; These, A.; Kupfer, C.; Hu, H.; Awais, M.; Saidaminov, M.; Dar, M. I.; Brabec, C.; Satapathi, S. Advances in Lead-Free Perovskite Single Crystals: Fundamentals and Applications. *ACS Mater. Lett.* **2021**, *3*, 1025−1080.

(6) Gao, Y.; Huang, C.; Hao, C.; Sun, S.; Zhang, L.; Zhang, C.; Duan, Z.; Wang, K.; Jin, Z.; Zhang, N.; Kildishev, A. V.; Qiu, C.-W.; Song, Q.; Xiao, S. Lead Halide Perovskite Nanostructures for Dynamic Color Display. *ACS Nano* **2018**, *12*, 8847−8854.

(7) Jeon, N. J.; Noh, J. H.; Kim, Y. C.; Yang, W. S.; Ryu, S.; Seok, S. I. Solvent Engineering for High-Performance Inorganic-Organic Hybrid Perovskite Solar Cells. *Nat. Mater.* **2014**, *13*, 897−903.

(8) Xing, G.; Mathews, N.; Lim, S. S.; Yantara, N.; Liu, X.; Sabba, D.; Grätzel, M.; Mhaisalkar, S.; Sum, T. C. Low-Temperature Solution-Processed Wavelength-Tunable Perovskites for Lasing. *Nat. Mater.* **2014**, *13*, 476−480.

(9) Marçal, L. A. B.; Benter, S.; Irish, A.; Dzhigaev, D.; Oksenberg, E.; Rothman, A.; Sanders, E.; Hammarberg, S.; Zhang, Z.; Sala, S.; Björling, A.; Unger, E.; Mikkelsen, A.; Joselevich, E.; Timm, R.; Wallentin, J. Inducing Ferroelastic Domains in Single-Crystal CsPbBr3 Perovskite Nanowires Using Atomic Force Microscopy. *Phys. Rev. Mater.* **2021**, *5*, L063001.

(10) Zhang, X.; Wang, F.; Zhang, B.-B.; Zha, G.; Jie, W. Ferroelastic Domains in a CsPbBr3 Single Crystal and Their Phase Transition Characteristics: An in-situ TEM Study. *Cryst. Growth Des.* **2020**, *20*, 4585−4592.

(11) Rothmann, M. U.; Li, W.; Zhu, Y.; Bach, U.; Spiccia, L.; Etheridge, J.; Cheng, Y.-B. Direct Observation of Intrinsic Twin Domains in Tetragonal CH3NH3PbI3. *Nat. Commun.* **2017**, *8*, 14547.

(12) Röhm, H.; Leonhard, T.; Schulz, A. D.; Wagner, S.; Hoffmann, M. J.; Colsmann, A. Ferroelectric Properties of Perovskite Thin Films and Their Implications for Solar Energy Conversion. *Adv. Mater.* **2019**, *31*, 1806661.

(13) Xiao, X.; Li, W.; Fang, Y.; Liu, Y.; Shao, Y.; Yang, S.; Zhao, J.; Dai, X.; Zia, R.; Huang, J. Benign Ferroelastic Twin Boundaries in Halide Perovskites for Charge Carrier Transport and Recombination. *Nat. Commun.* **2020**, *11*, 2215.

(14) Bharadwaj, P.; Deutsch, B.; Novotny, L. Optical Antennas. *Adv. Opt. Photonics* **2009**, *1*, 438−483.

(15) Alaei, A.; Circelli, A.; Yuan, Y.; Yang, Y.; Lee, S. S. Polymorphism in Metal Halide Perovskites. *Mater. Adv.* **2021**, *2*, 47−63.

(16) Yi, J.; Ge, X.; Liu, E.; Cai, T.; Zhao, C.; Wen, S.; Sanabria, H.; Chen, O.; Rao, A. M.; Gao, J. The Correlation between Phase Transition and Photoluminescence Properties of CsPbX3 (X = Cl, Br, I) Perovskite Nanocrystals. *Nanoscale Adv.* **2020**, *2*, 4390−4394.

(17) Zhang, L.; Zeng, Q.; Wang, J. Pressure-Induced Structural and Optical Properties of Inorganic Halide Perovskite CsPbBr3. *J. Phys. Chem. Lett.* **2017**, *8*, 3752−3758.

(18) Mannino, G.; Deretzis, I.; Smecca, E.; La Magna, A.; Alberti, A.; Ceratti, D.; Cahen, D. Temperature-Dependent Optical Band Gap in

CsPbBr3, MAPbBr3, and FAPbBr3 Single Crystals. *J. Phys. Chem. Lett.* **2020**, *11*, 2490−2496.
(19) Ghaithan, H. M.; Alahmed, Z. A.; Qaid, S. M. H.; Hezam, M.; Aldwayyan, A. S. Density Functional Study of Cubic, Tetragonal, and Orthorhombic CsPbBr3 Perovskite. *ACS Omega* **2020**, *5*, 7468−7480.
(20) Dobrovolsky, A.; Merdasa, A.; Unger, E. L.; Yartsev, A.; Scheblykin, I. G. Defect-Induced Local Variation of Crystal Phase Transition Temperature in Metal-Halide Perovskites. *Nat. Commun.* **2017**, *8*, 34.
(21) Jin, H.; Debroye, E.; Keshavarz, M.; Scheblykin, I. G.; Roeffaers, M. B. J.; Hofkens, J.; Steele, J. A. It's a Trap! On the Nature of Localised States and Charge Trapping in Lead Halide Perovskites. *Mater. Horiz.* **2020**, *7*, 397−410.
(22) Eaton, S. W.; Laia, M.; Gibson, N. A.; Wong, A. B.; Dou, L.; Ma, J.; Wang, L.-W.; Leone, S. R.; Yang, P. Lasing in Robust Cesium Lead Halide Perovskite Nanowires. *Proc. Natl. Acad. Sci. U. S. A.* **2016**, *113*, 1993−1998.
(23) Berestennikov, A. S.; Voroshilov, P. M.; Makarov, S. V.; Kivshar, Y. S. Active Meta-Optics and Nanophotonics with Halide Perovskites. *Appl. Phys. Rev.* **2019**, *6*, 031307.
(24) Govorov, A. O.; Richardson, H. H. Generating Heat with Metal Nanoparticles. *Nano Today* **2007**, *2*, 30−38.
(25) Baffou, G.; Quidant, R.; de Abajo, F. J. G. Nanoscale Control of Optical Heating in Complex Plasmonic Systems. *ACS Nano* **2010**, *4*, 709−716.
(26) Baffou, G.; Cichos, F.; Quidant, R. Applications and challenges of thermoplasmonics. *Nat. Mater.* **2020**, *19*, 946−958.
(27) Zograf, G. P.; Petrov, M. I.; Makarov, S. V.; Kivshar, Y. S. All-Dielectric Thermonanophotonics. *Adv. Opt. Photonics* **2021**, *13*, 643−702.
(28) Lee, W.; Li, H.; Wong, A. B.; Zhang, D.; Lai, M.; Yu, Y.; Kong, Q.; Lin, E.; Urban, J. J.; Grossman, J. C.; Yang, P. Ultralow Thermal Conductivity in All-Inorganic Halide Perovskites. *Proc. Natl. Acad. Sci. U. S. A.* **2017**, *114*, 8693−8697.
(29) Kharintsev, S. S.; Kharitonov, A. V.; Chernykh, E. A.; Alekseev, A. M.; Filippov, N. A.; Kazarian, S. G. Designing Two-Dimensional Temperature Profiles Using Tunable Thermoplasmonics. *Nanoscale* **2022**, *14*, 12117−12128.
(30) Kharintsev, S. S.; Chernykh, E. A.; Shelaev, A. V.; Kazarian, S. G. Nanoscale Sensing Vitrification of 3D Confined Glassy Polymers through Refractory Thermoplasmonics. *ACS Photonics* **2021**, *8*, 1477−1488.
(31) Kharintsev, S. S.; Kazarian, S. G. Nanoscale Melting of 3D Confined Azopolymers through Tunable Thermoplasmonics. *J. Phys. Chem. Lett.* **2022**, *13*, 5351−5357.
(32) Ishii, S.; Higashino, M.; Goya, S.; Shkondin, E.; Tanaka, K.; Nagao, T.; Takayama, O.; Murai, S. Extreme Thermal Anisotropy in High-Aspect-Ratio Titanium Nitride Nanostructures for Efficient Photothermal Heating. *Nanophotonics* **2021**, *10*, 1487−1494.
(33) Liao, M.; Shan, B.; Li, M. In Situ Raman Spectroscopic Studies of Thermal Stability of All-Inorganic Cesium Lead Halide (CsPbX3, X = Cl, Br, I) Perovskite Nanocrystals. *J. Phys. Chem. Lett.* **2019**, *10*, 1217−1225.
(34) Zhao, Z.; Zhong, M.; Zhou, W.; Peng, Y.; Yin, Y.; Tang, D.; Zou, B. Simultaneous Triplet Exciton−Phonon and Exciton−Photon Photoluminescence in the Individual Weak Confinement CsPbBr3Micro/Nanowires. *J. Phys. Chem. C* **2019**, *123*, 25349−25358.
(35) Chen, T.; Wang, C.; Xing, X.; Qin, Z.; Qin, F.; Wang, Y.; Alam, M. D.; Hadjiev, V. G.; Yang, G.; Ye, S.; Yang, J.; Wang, R.; Yue, S.; Zhang, D.; Shang, Z.; Robles-Hernandez, F. C.; Calderon, H. A.; Wang, H.; Wang, Z.; Bao, J. Integration of Highly Luminescent Lead Halide Perovskite Nanocrystals on Transparent Lead Halide Nanowire Waveguides through Morphological Transformation and Spontaneous Growth in Water. *Small* **2022**, *18*, 2105009.
(36) Khmelevskaia, D.; Markina, D.; Tonkaev, P.; Masharin, M.; Peltek, A.; Talianov, P.; Baranov, M. A.; Nikolaeva, A.; Zyuzin, M. V.; Zelenkov, L. E.; Pushkarev, A. P.; Rogach, A. L.; Makarov, S. V. Excitonic versus Free-Carrier Contributions to the Nonlinearly Excited Photoluminescence in $CsPbBr_3$ Perovskites. *ACS Photonics* **2022**, *9*, 179−189.
(37) Zhu, Y.; Cui, Q.; Chen, J.; Chen, F.; Shi, Z.; Zhao, X.; Xu, C. Inhomogeneous Trap-State-Mediated Ultrafast Photocarrier Dynamics in CsPbBr3Microplates. *ACS Appl. Mater. Interfaces* **2021**, *13*, 6820−6829.
(38) Chen, F.; Zhu, C.; Xu, C.; Fan, P.; Qin, F.; Manohari, A. G.; Lu, J.; Shi, Z.; Xu, Q.; Pan, A. Crystal Structure and Electron Transition Underlying Photoluminescence of Methylammonium Lead Bromide Perovskites. *J. Mater. Chem.C* **2017**, *5*, 7739−7745.
(39) Shanks, H. R.; Maycock, P. D.; Sidles, P. H.; Danielson, G. C. Thermal Conductivity of Silicon from 300 to 1400 K. *Phys. Rev.* **1963**, *130*, 1743−1748.
(40) Pushkarev, A. P.; Korolev, V. I.; Markina, D. I.; Komissarenko, F. E.; Naujokaitis, A.; Drabavičius, A.; Pakštas, V.; Franckevičius, M.; Khubezhov, S. A.; Sannikov, D. A.; Zasedatelev, A. V.; Lagoudakis, P. G.; Zakhidov, A. A.; Makarov, S. V. A Few-Minute Synthesis of CsPbBr3 Nanolasers with a High Quality Factor by Spraying at Ambient Conditions. *ACS Appl. Mater. Interfaces* **2019**, *11*, 1040−1048.

https://doi.org/10.1021/acsnano.3c00373
ACS Nano 2023, 17, 9235−9244